PHOTONICS Research

Nonlinear dynamics in a circular-sided square microcavity laser

Jian-Cheng Li,[1,2] 🄳   Jin-Long Xiao,[1,2] 🄳   Yue-De Yang,[1,2] 🄳   You-Ling Chen,[1,2] 🄳
and Yong-Zhen Huang[1,2,*] 🄳

[1]*State Key Laboratory of Integrated Optoelectronics, Institute of Semiconductors, Chinese Academy of Sciences, Beijing 100083, China*
[2]*Center of Materials Science and Optoelectronics Engineering, University of Chinese Academy of Sciences, Beijing 100049, China*
Corresponding author: yzhuang@semi.ac.cn

Self-chaotic dual-mode and tri-mode microcavity lasers have been recently proposed and demonstrated for high-speed random number generation. Here, we report the characteristics of irregular pulse packages and self-chaos operation for a dual-mode circular-sided square microcavity laser. In addition to the mode interaction between the fundamental and first-order transverse modes, we observed irregular pulse packages due to the mode beating of near-degenerate modes for the first time to our best knowledge. Moreover, a successive route from periodic-one and periodic-three states to chaos is first experimentally illustrated by increasing injection current. The chaotic state is observed over a current range of 10 mA, and the maximum chaos effective bandwidth of 22.4 GHz is realized with a flatness of ±4 dB. Chaotic characteristics are also investigated for different longitudinal modes, which indicates that the self-chaotic microlaser can provide robust parallel chaotic outputs for practical application.   © 2023 Chinese Laser Press

https://doi.org/10.1364/PRJ.489371

1. INTRODUCTION

Optical chaos has attracted great attention for significant applications, such as physical random number generation [1,2], secure communication [3], optical time-domain reflectometry [4], chaotic radar [5,6], and reservoir computing [7], owing to its characteristics of randomness, high sensitivity to initial conditions, and broad radio-frequency (RF) spectrum [8]. Semiconductor lasers belonging to Class B lasers, with dynamics governed by two equations for the field and population inversion, are stable in nature [9]. In order to destabilize the semiconductor lasers for chaos generation, external perturbations are usually required, such as optical injection [10–12], mutual injection [13], optical or optoelectronic feedback [14–17], and mixed disturbance [18,19]. However, semiconductor laser chaos systems consisting of discrete optical components and devices are cumbersome and susceptible to environmental disturbance.

To meet the demand of miniaturization and stability, various integrated chaotic semiconductor lasers have been developed for random number generation. Argyris *et al.* reported an integrated chaotic distributed feedback (DFB) laser with a phase section and long passive waveguide [20]. Tronciu *et al.* presented a monolithic high-dimensional chaos source under multiple optical feedback loops with an air gap [21]. Harayama *et al.* integrated a DFB laser with two semiconductor optical amplifiers, a photoelectric detector, and a linear or ring passive optical waveguide for strong optical feedback [22,23]. Wu *et al.* reported a three-section

integrated chaotic semiconductor laser chip, composed of a DFB section, a phase section, and an amplification section [24]. Zhang *et al.* demonstrated a hybrid integrated short external cavity and wavelength-tunable monolithically chaotic semiconductor lasers [25,26]. In addition, optical mutual injection integrated chips by coupled distributed Bragg reflector (DBR), DFB, and microring lasers were fabricated for investigating nonlinear dynamics, including the chaos state [27–29]; however, small parameter ranges for the chaotic state failed to be resolved.

In addition to the integrated chaotic semiconductor lasers, new mechanisms were investigated for opening a new pathway for chaotic semiconductor lasers. A deterministic polarization chaos without external perturbation was observed in vertical-cavity surface-emitting lasers (VCSELs), where two polarized modes experience nonlinear coupling by mode competition [30]. Recently, circular-sided hexagonal chaotic microlasers were reported due to the internal mode interaction of two transverse modes [31]. Further, a chaotic bandwidth enhancement was illustrated by photon-photon resonance in a tri-mode deformed square microcavity laser [32]. Based on a wide-bandwidth self-chaotic microcavity laser, random bit generation at 400 Gb/s by retaining multiple least significant bits was demonstrated [33]. Compared with integrated chaos chips and self-chaotic VCSELs, self-chaotic microcavity lasers require a simple process without repeated epitaxy and are easy to mass produce with low cost.

However, the transverse mode field distributions of a hexagonal microcavity are narrower than that of square microcavity, and the cross coefficient between the mode field patterns of the fundamental and first-order transverse modes in a hexagonal microcavity is more complicated than that in a square microcavity. Thus, the space carrier oscillation caused by stimulated emission of beating intensity of the fundamental and first-order transverse modes in a hexagonal microcavity is much weaker than that in a square microcavity. We can expect that a square microcavity laser is easier to realize self-nonlinear dynamical states due to mode interaction between the fundamental and first-order transverse modes. In this paper, we demonstrate the evolution of nonlinear dynamical states due to dual-mode interaction and the effect of near-degenerate modes in a circular-sided square semiconductor microcavity laser. First, mode characteristics are designed for a deformed square microcavity with a larger inner-diameter hole than that in Ref. [32], and circular-sided square microcavity semiconductor lasers are fabricated. Then, an irregular pulse-package phenomenon is first observed in a dual-mode microlaser, which can be attributed to the effect of near-degenerate mode beating. Furthermore, the evolution route from period-one and period-three states to chaos is clearly observed with the increase of injection current, due to the adjustment of mode interval, for the microcavity laser. Correspondingly, the chaotic effective RF bandwidth is 22.4 GHz with the flatness of ± 4 dB, and the chaos operation current range is up to 10 mA. In addition, chaos characteristics for different longitudinal modes and all modes are comparatively investigated. New findings have shown stronger superiority and potential for practical application.

2. NUMERICAL SIMULATION

Dual-mode microcavity lasers with a mode interval about 10 GHz or less can result in plenty of nonlinear dynamic phenomena due to strong nonlinear mode interaction accompanying carrier oscillation [31]. The in-phase and antiphase sections are formed by the different spatial mode field distributions of two transverse modes. When the mode interval is below the relaxation oscillation frequency, carrier density can oscillate dramatically with the mode-beating, and an internal optical-injection perturbation is obtained with side peak of the lasing mode caused by the oscillation as an injection term for another lasing mode. Consequently, chaotic dynamics could spontaneously be generated due to carrier oscillation at beating frequency and the internal injection between the two lasing modes. To realize a mode interval near the potential value of the relaxation frequency, a circular-sided square microcavity with a central hole is numerically investigated by a 2D finite element method (via commercial software COMSOL Multiphysics), for transverse electric modes. The 3D schematic diagram of the microcavity is shown in Fig. 1(a), with the 2D simulation schematic diagram in Fig. 1(b), where a, r, d, h, and R_{in} are the flat-side length of square, the radius of the circular arc, the width of output waveguide, the shift distance of the waveguide, and the radius of central hole, respectively. The circular-sided deformation parameter is defined as $\delta = r - \sqrt{r^2 - a^2/4}$, and a 1 μm wide perfectly matched layer (PML) is utilized to terminate the simulation window. In the simulation, the refractive indices of InP-based microcavity and surrounding bisbenzocyclobutene (BCB) material are set to 3.2 and 1.54, respectively.

Tri-mode chaotic operation for random bit generation was achieved for the circular-sided square cavity with $a = 20$ μm, $\delta = 2.17$ μm, $d = 1.5$ μm, $h = 4\sqrt{2}$ μm, and $R_{in} = 5.5$ μm in Ref. [32]. Here, we further increase the radius of circle hole R_{in} to 6.5 μm with other parameters unaltered for dual-transverse-mode lasing, for clearly examining the effect of near-degenerate modes. As shown in Fig. 1(c), the mode Q-factors of the fundamental (0th) and first-order (1st) transverse modes are 1.4×10^5 and 2.0×10^4 at the wavelength of 1550.111 and 1550.154 nm, respectively, and the Q-factor of the second-order transverse mode is only about 3.0×10^3. The magnetic field ($|H_z|$) distributions for the 0th and 1st modes with the high Q-factor are shown in the insets of Fig. 1(c), where the output waveguide squeezes and partly releases the mode fields near the connected position, resulting in the tilted and broadened mode profiles near the midpoints of adjacent sides. The mode fields of the transverse modes for the circulated-side square microcavity with a connecting waveguide can be explained by expanding the wave function in cylindrical [34]. Further, the parameters $|\alpha_m|^2$ of different angular quantum numbers m for the high Q-factor 0th mode are shown in Fig. 1(d), where positive and negative values of m are corresponding to counterclockwise (CCW) and clockwise (CW) waves, respectively. The Husimi distribution maps for near-degenerate modes with the high Q-factor are illustrated in Figs. 1(e) and 1(f), respectively. The negative and positive values of $\sin \chi$ correspond to the CW and CCW mode in resonant cavity, respectively. We can find eight islands in Figs. 1(e) and 1(f), and the calculated eigenvalues of the monodromy matrix $\begin{bmatrix} 0.0089 & -1.4142 \\ 0.7070 & 0.0089 \end{bmatrix}$ for the 0th and 1st modes are complex conjugate, i.e., $0.0089 \pm i$, which indicate that these four-bounce diamond periodic orbit modes are stable in the microcavity [35,36]. The intensity of the down islands is larger than that of the upper islands, which is consistent with the domination of the CW mode. The mode interval of 5.1 GHz between the 0th and 1st mode is suitable for realizing strong nonlinear dynamics, and the simulated free spectrum range is about 10.8 nm. A ring p-electrode with a width of $w = 4$ μm is designed to achieve nonuniform current injection, which may modulate the carrier and temperature distributions inside the resonator, for finely tuning mode interval. To account for the effect of the ring electrode, a refractive index step Δn is simply used between inner and outer of the injected window [37], which results in the variation of mode frequency interval with the injection current. The simulated mode Q-factors and mode intervals $\Delta f_{01} = f_{0th} - f_{1st}$, $\Delta f_{00} = f_{0S} - f_{0L}$, and $\Delta f_{11} = f_{1S} - f_{1L}$ versus the refractive index variation Δn are plotted in Figs. 1(g)–1(i), in which the subscripts S and L stand for the short- and long-wavelength mode of near-degenerate modes, respectively. In the range $-0.005 < \Delta n < 0.01$, the mode interval Δf_{01} varies linearly with Δn, and the maximum mode interval between near-degenerate modes Δf_{00} and Δf_{11} can reach 280 MHz and 1.3 GHz, respectively.
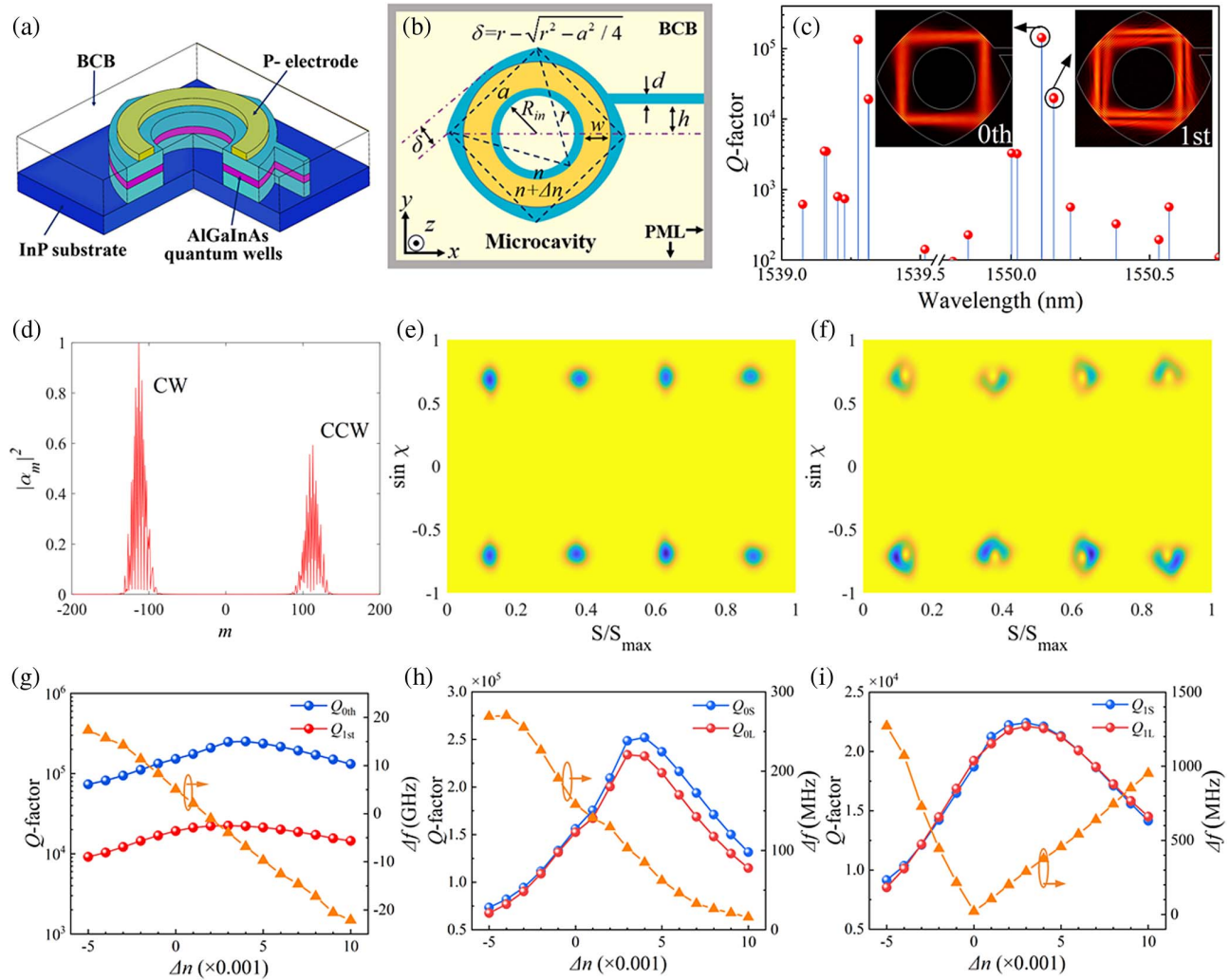
Fig. 1. (a) 3D schematic diagram of a microcavity laser with a quarter deleted. (b) 2D simulated diagram of circular-sided square microcavity with a central hole. (c) Mode Q-factor versus mode wavelength. Insets are magnetic field ($|H_z|$) distributions for the 0th and 1st transverse modes. (d) $|\alpha_m|^2$ of different angular quantum numbers m for the high Q-factor 0th mode. Husimi distribution map in a circular-sided square microcavity with an output waveguide for the (e) 0th and (f) 1st near-degenerate modes with the high Q-factor. Mode Q-factor and mode frequency interval Δf versus the change of refractive index Δn for (g) high-Q 0th mode and 1st mode, (h) two near-degenerate modes of the 0th mode, and (i) two near-degenerate modes of the 1st mode.

3. EXPERIMENTAL RESULTS

A. Process and Static Property

The circular-side square microcavity lasers were fabricated using an AlGaInAs/InP epitaxial wafer consisting of six pairs of compressively strained multiple-quantum-wells (MQWs). A SiO$_2$ layer as a hard mask for cavity etching was first deposited using plasma-enhanced chemical vapor deposition. Contacting photolithography and inductively coupled plasma (ICP) were employed to transfer the microcavity patterns onto the SiO$_2$ layer, and the laser wafer is then etched to 4.3 μm by ICP process again. Then, the BCB layer with low permittivity was utilized to achieve lateral confinement and surface planarization. After that, a ring Ohmic contact window is opened on the top of the resonator; further, a patterned Ti/Pt/Au p-electrode and an Au/Ge/Ni n-type backside electrode were evaporated.

We have fabricated microlasers with designed parameters $a = 20$ μm, $\delta = 2.17$ μm, $d = 1.5$ μm, $R_{in} = 6.5$ μm, $h = 4\sqrt{2}$ μm, and $w = 4.0$ μm. The microscope image of a microlaser is shown in the inset of Fig. 2(a). The devices are cleaved over the output waveguide and mounted on a thermoelectric cooler with a constant temperature at 289 K for testing. The output power collected by a tapered single-mode fiber (SMF) as well as the applied voltage versus the continuous-wave (CW) injection current is plotted in Fig. 2(a). The threshold current is about 4 mA verified from the lasing spectra, corresponding to the threshold current density of 1.68kA/cm^2, and the maximum of SMF coupled power is 49 μW at 42 mA. The power-current relation is influenced by lasing mode jumping and heating effect. The series resistance of the laser is estimated to be 22.8 Ω from V-I curve. The power kink point at 26 mA in Fig. 2(a) is due to chaotic nonlinearity [9,38], which is
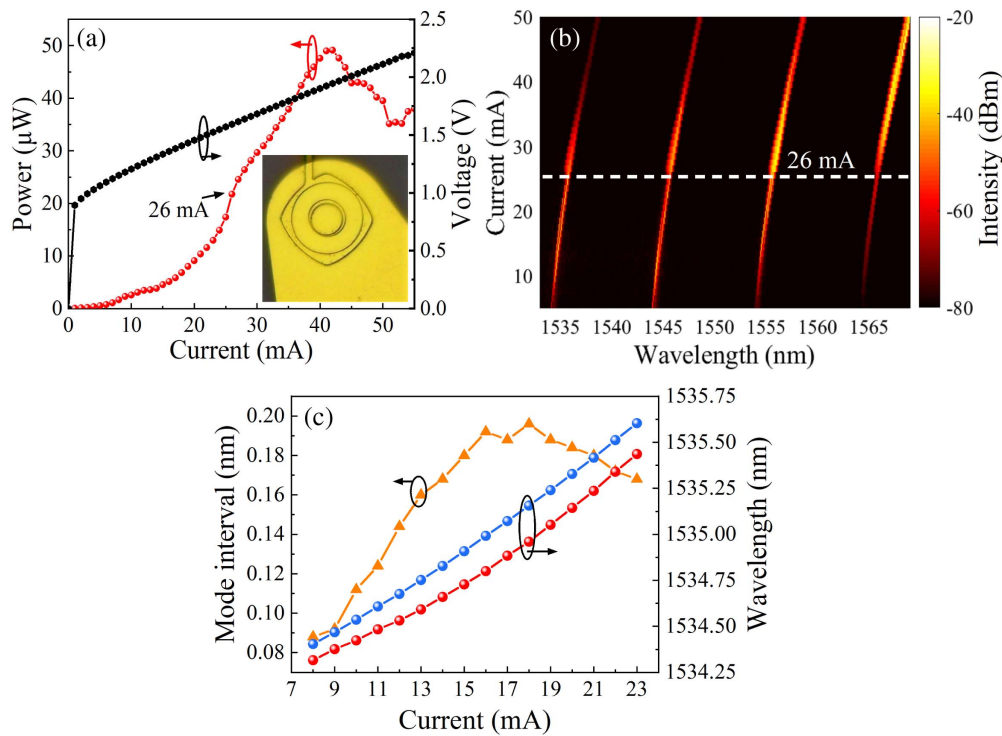
Fig. 2. (a) Output power coupled into an SMF and the applied voltage versus the CW injection current. (b) Lasing spectra map and (c) lasing mode wavelengths and mode intervals versus the CW injection current. Inset in (a): microscope image of a circular-sided square microlaser.

corresponding to a wide lasing peak above 26 mA indicated by the lasing spectral map versus the current in Fig. 2(b). A broadened lasing peak owing to the presence of several nonresolved lasing peaks is observed for lasing mode around 1555 nm over a current range of 10 mA. Figure 2(c) shows the mode wavelengths around 1535 nm and corresponding mode intervals with regarding to the injection current. The mode interval increases with the injection current from 8 to 16 mA, which is corresponding to the decrease of Δn by comparing with Fig. 1(g). When the injection current ranges from 16 to 23 mA, the mode interval becomes saturated and slightly decreases, accompanied with complex nonlinearity.

B. Irregular Pulse Packages

Nonlinear dynamics of the microlaser were measured using a test system, as shown in Fig. 3(a). The laser output signal was collected by an SMF and an optical isolator was utilized to avoid unwanted optical feedback. An optical spectrum analyzer (Yokogawa, AQ6370D, 0.02 nm resolution), an electrical spectrum analyzer (Rohde & Schwarz FSW50), and a real-time oscilloscope (Tektronix DPO77002SX, 33 GHz bandwidth, 100 GSa/s) were used to measure lasing spectra, RF spectra, and real-time waveform of the laser output. An erbium-doped fiber amplifier and a tunable optical bandpass filter (OBPF) were used for optical amplification and selecting the output of different longitudinal modes. The OBPF was removed from the test system when investigating the output characteristics of all longitudinal modes. A bias-T (SHF BT45R, 20 kHz to 45 GHz) was introduced to extract AC components of converted electrical signal from a high-speed photodetector (Finisar XPDV2120R, 50 GHz bandwidth).

First, a temporal irregular pulse-package phenomenon ranging from 15 to 22 mA is recognized and investigated. Optical spectra of two groups of longitudinal modes are illustrated in Fig. 3(b) at 18, 20, and 22 mA. For longitudinal mode around 1545 nm, the intensity of the 1st mode (long-wavelength mode) is higher than that of the 0th mode (short-wavelength mode); the mode position is assigned based on the simulation results shown in Fig. 1(c). The relative relationship between orders and wavelengths is applicable to different longitudinal modes and different currents. When the current is 22 mA, two near-degenerate modes at 1545.376 and 1545.436 nm are clearly distinguished for the 1st mode. The RF spectra for this group longitudinal mode are shown in Fig. 3(c), and a peak around 7 GHz owing to mode beating of the near-degenerate modes is increased with the current from 18 to 22 mA. In order to distinguish details, the RF spectra at 20 and 22 mA are moved up 5 and 10 dB in Figs. 3(c)–3(e), respectively. For the lasing spectra of another longitudinal mode around 1555 nm, the mode intervals for 0th and 1st modes are about 0.204, 0.176, and 0.168 nm at 18, 20, and 22 mA, respectively, corresponding to the strong beating peaks around 25, 22, and 21 GHz in the RF spectra shown in Fig. 3(d). In addition, low-frequency harmonics are also observed in the dotted box in Fig. 3(d), as reported in the case of short-cavity feedback [39,40], and a local enlarged view is displayed in Fig. 3(e). The fundament harmonic frequency is 0.58, 0.68, and 0.84 GHz at 18, 20, and 22 mA. These low-frequency peaks are caused by two near-degenerate modes of 0th mode (around 1554.884 nm), recognized by wider linewidth in lasing spectra compared with the 1st mode in Fig. 3(b). Because the
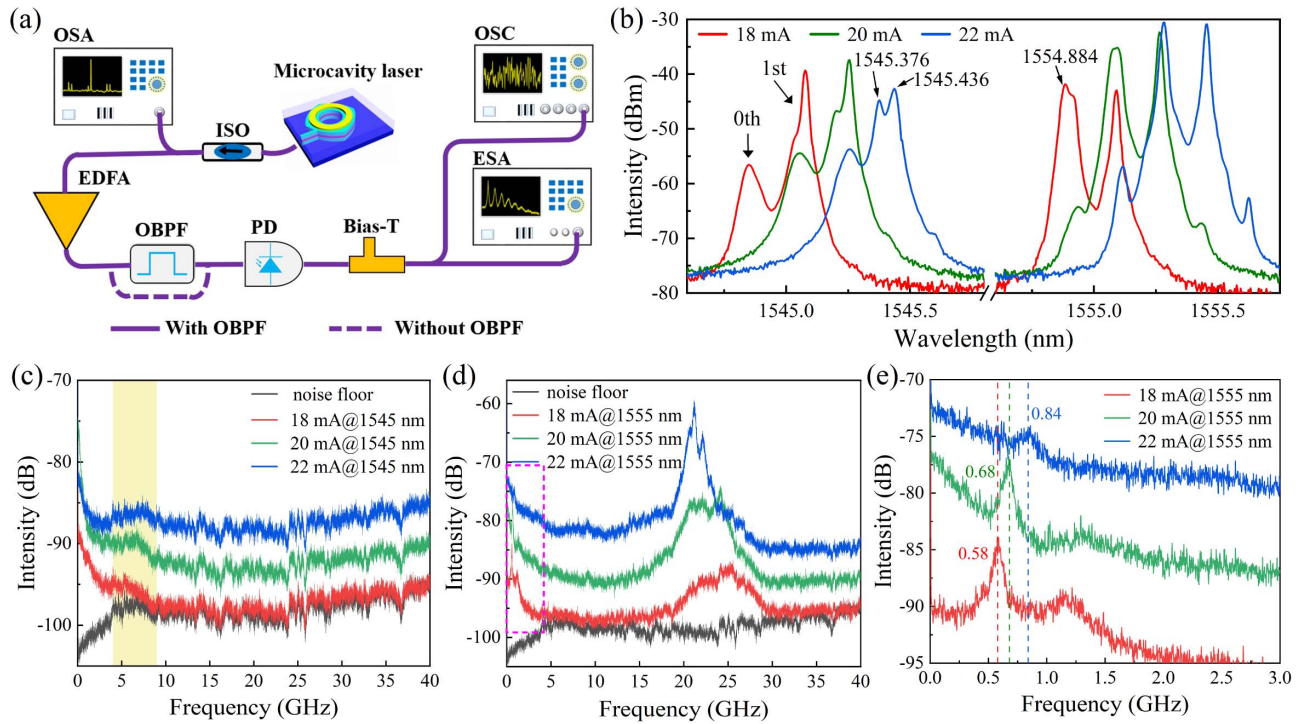
Fig. 3. (a) Test system for nonlinear dynamics. ISO, isolator; OSA, optical spectrum analyzer; EDFA, erbium-doped fiber amplifier; OBPF, optical bandpass filter; PD, photodetector; ESA, electrical spectrum analyzer; OSC, real-time oscilloscope. (b) Lasing spectra and RF spectra for longitudinal mode around (c) 1545 nm and (d) 1555 nm, at currents of 18, 20, and 22 mA. (e) Enlarged view of RF spectra in dotted box in (d).

length of output waveguide is about 10–20 μm, corresponding to a delayed frequency of ∼THz, these low-frequency harmonics are not caused by parasitic feedback at the cleaved output of the waveguide. Mode beating of different near-degenerate modes of the fundamental and 1st order transverse modes also accounts for the complex multipeak structure around 21–25 GHz, as shown in Fig. 3(d). Figure 4 presents the temporal behavior of the AC component of laser output at 20 mA. The signal intensity increases abruptly and then decreases gradually to the lowest value marked by blue lines. The repeated process forms a pulse intensity envelope modulated by the low-frequency component related to the mode beating of the near-degenerate modes of the 0th mode in Figs. 3(d) and 3(e). The time interval of two adjacent envelope peaks in Fig. 4 is 1.5 ns or so, which is coincident with the 0.68 GHz frequency peak at 20 mA in Fig. 3(e). Moreover, we can find the low-frequency envelope is separated by a shorter time interval, which corresponds to the high-frequency oscillations around 22–24 GHz, as shown in Fig. 3(d). Consequently, the whole pulse packages are not regular owing to these irregular high-frequency oscillations.

C. Chaos Dynamics

More complex nonlinear phenomena originating from dual-transverse-mode interaction are achieved by further increasing current for the deformed square microlaser. The detailed evolving route into chaotic state is illustrated by the optical spectra and RF spectra, as shown in Figs. 5(a)–5(d), at the injection currents of 23, 24, 25, and 26 mA, respectively. The RF spectra were measured by filtering the main longitudinal mode around

1555 nm, with the black line of the noise floor of electrical spectrum analyzer.

At 23 mA, two main modes at 1555.380 and 1555.552 nm with two side peaks at 1555.208 and 1555.724 nm are observed in Fig. 5(a1). The adjacent mode interval is 0.172 nm, in agreement with the sharp peaks at 21.37 GHz in Fig. 5(a2), which indicates the microlaser in the periodic-one (P1) state. At 24 mA, a narrower beating peak at 21.60 GHz and its harmonic at 43.16 GHz (enlarged view in dotted box) are observed in Fig. 5(b2). Moreover, two weak peaks with comparable intensity at 7.19 and 14.38 GHz occur, corresponding to one-third and two-thirds resonance frequency of the peak frequency of 21.60 GHz. The frequency of 7.19 GHz originates
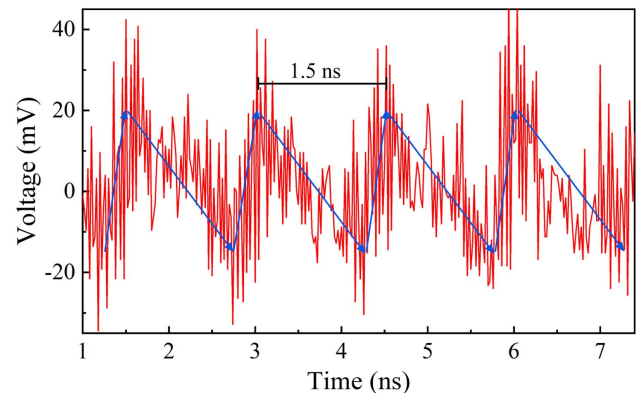

Fig. 4. Temporal dynamics for irregular pulse packages of the longitudinal mode around 1555 nm for the microlaser at 20 mA.
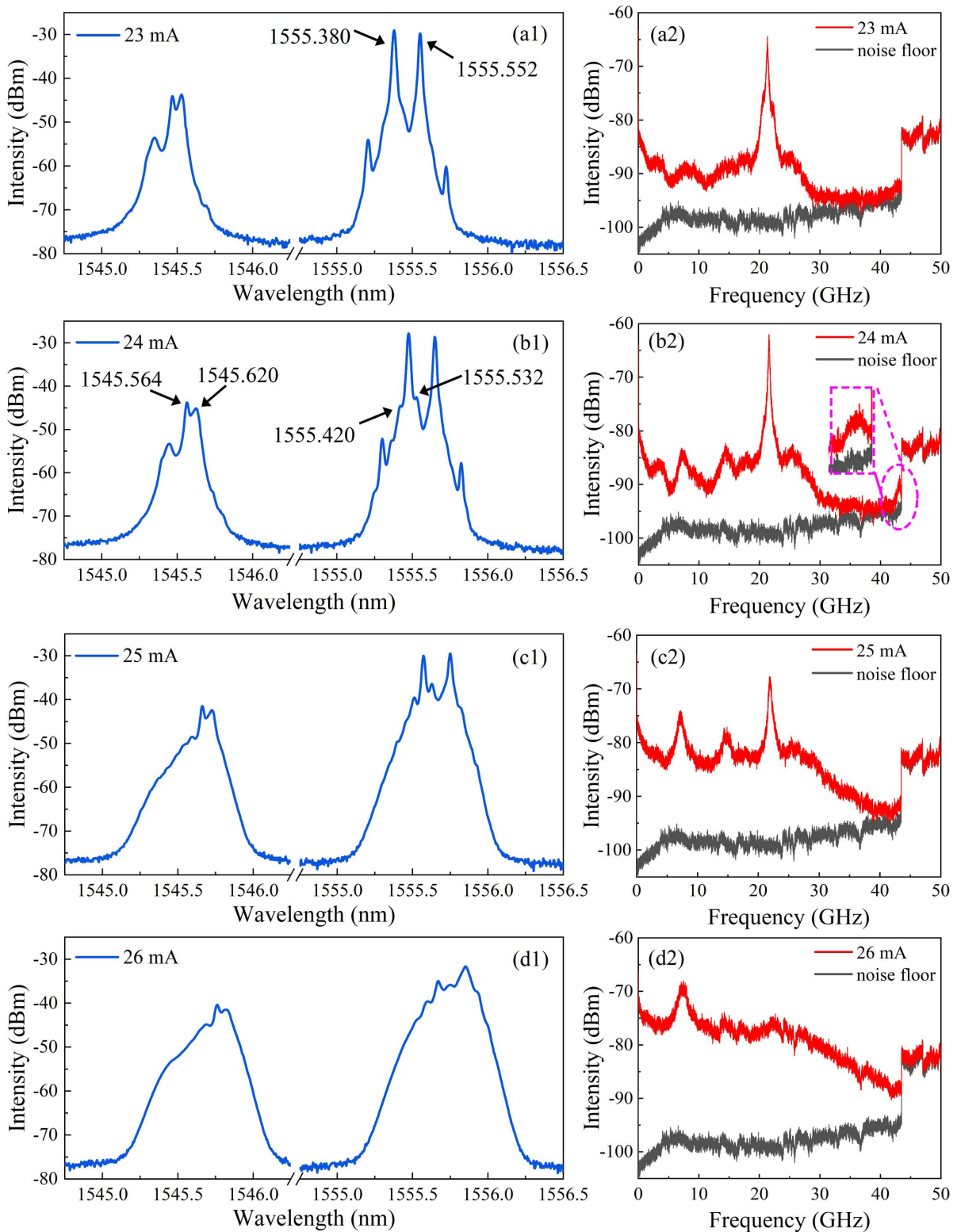
Fig. 5. Dynamic routes into the chaotic state around 1555 nm for dual-transverse-mode self-chaotic microlaser: (a) P1 state at 23 mA, (b) P3 state at 24 mA, (c) P3 plus chaos at 25 mA, and (d) chaos at 26 mA. (a1)–(d1) Lasing spectra and (a2)–(d2) corresponding RF spectra.

from the mode-beating modulation of the 1st near-degenerate modes at 1545.564 and 1545.620 nm, owing to different longitudinal modes sharing carriers in the same microcavity. Due to oscillation coupling for the mode beatings between

near-degenerate modes around 1545 nm and the 0th and 1st transverse modes around 1555 nm, the microlaser provides obvious proof of the periodic-three (P3) oscillation. Meanwhile, we also find side-peaks at the wavelength of

1555.420 and 1555.532 nm around the short-wavelength mode at 1555.476 nm in Fig. 5(b1). At 25 mA, the RF peaks at 7.25 and 14.63 GHz become obvious, and the beating RF peak at 21.84 GHz reduces greatly, as shown in Fig. 5(c2); further, the RF energy is gradually transferred to the low-frequency region. In Fig. 5(c1), wide lasing spectra are observed for the longitudinal modes around 1545.5 and 1555.5 nm with strong side peaks around the main peak of 1555.5 nm. The wide and smooth lasing spectra are similar to those observed for chaotic states in Refs. [31,32]. The microlaser also operates at chaotic state with smooth and broadened lasing spectra, as shown in Fig. 5(d1), at 26 mA. The RF spectrum becomes flat, and the energy is distributed over a broad frequency range. As shown in Fig. 5(d2), the original sharp beating peak around 21 GHz disappears, and only a small peak at 7.35 GHz remains. The route of P1–P3-chaos is different from the route of P1-chaos illustrated in Refs. [31,32], and near-degenerate modes play a crucial role in chaos generation.

Further, the chaotic optical spectra from 27 to 35 mA are illustrated in Fig. 6(a). The chaotic operation range is about 10 mA, much larger than that about 3 mA in Ref. [31], which means stronger environment tolerance and a more robust chaos laser source. Specifically, we provide the RF spectra and time characteristics of AC component of the laser output at 29 mA, as shown in Figs. 6(b) and 6(c). Based on the definition in Ref. [41], the effective bandwidth is calculated as the sum of large discrete spectral segments of the chaotic power spectrum accounting for 80% of the total power, and the flatness

is defined as the intensity difference of the maximum to the minimum within the effective bandwidth. We obtained the effective bandwidth of 22.4 GHz and flatness of ±4 dB at 29 mA. Multimode chaos can effectively avoid the power drop of the RF spectrum ranging from DC to the relaxation oscillation frequency [42]. In terms of the bandwidth and flatness, to the best of our knowledge, the performance of this self-chaotic laser is superior to that reported in other solitary chaos lasers in Refs. [20–26]. The time-series presents an irregular oscillation and the autocorrelation function (ACF) in Fig. 6(d) decays rapidly like the delta function, with the half width at half maximum of 0.012 ns, without delayed peaks caused by optical feedback in Refs. [43–45]. A weak peak at 0.13 ns with ACF coefficient of 0.12 is corresponding to the reciprocal of the beating envelope peaks in Fig. 6(b). Due to the better RF spectrum flatness, the ACF curve does not have higher frequency oscillation below 0.13 ns, as shown in Ref. [32], which is beneficial for chaos detection and random bit generation. The calculated Wiener entropy from the time series is −1.1 dB, near 0 dB corresponding to the characteristic of the white noise, which indicates a great uniform of energy distribution [46].

For the self-chaotic microlaser, we also show the result of relative intensity noise (RIN) at 29 mA in Fig. 7 with the measurement technique in Ref. [47]. When the laser is operating chaotically, the RIN spectrum shares similar shape to RF spectrum in Fig. 6(b) with intensity value around −105 dB/Hz below 20 GHz. The higher RIN value at chaotic state is owing to complex nonlinear interaction of many mode components.
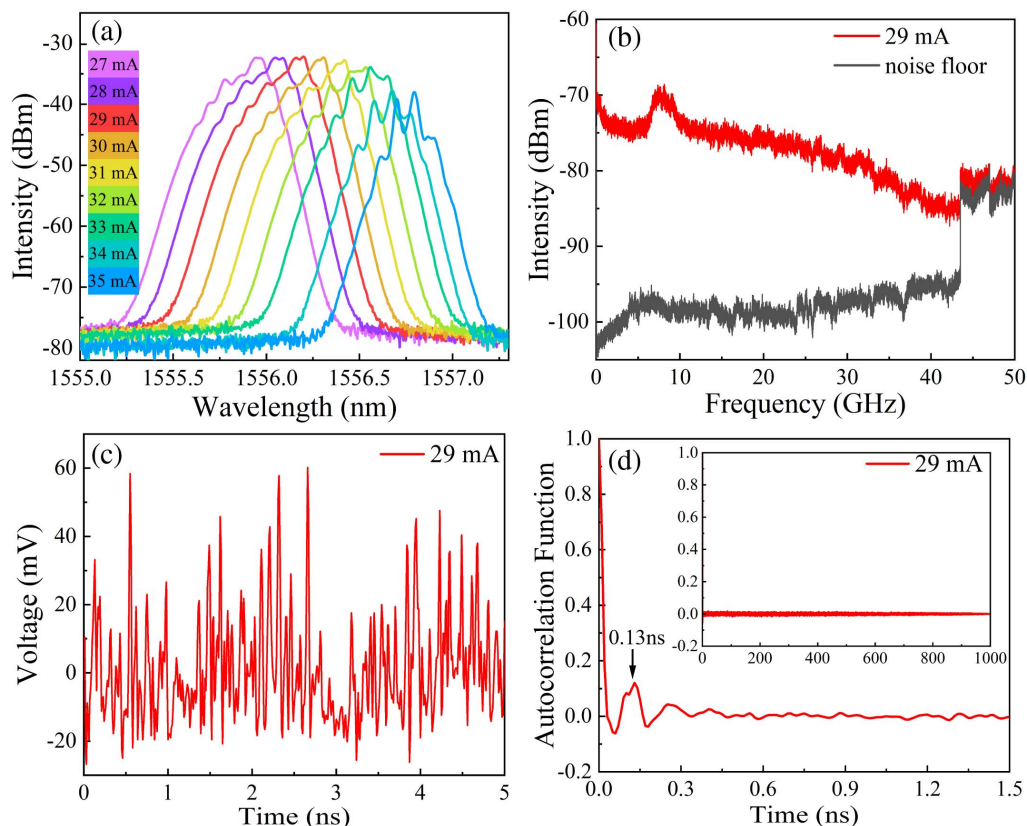

Fig. 6.   (a) Chaotic optical spectra with currents ranging from 27 to 35 mA. (b) RF spectrum, (c) temporal waveform, and (d) autocorrelation function of chaos signal at 29 mA by filtering the main longitudinal mode around 1556 nm. Inset in (d) is an ACF curve for 1000 ns.
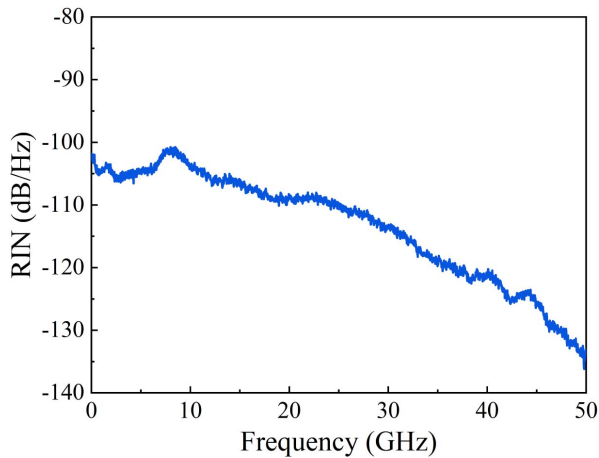
Fig. 7. Relative intensity noise of the self-chaotic microlaser at 29 mA.

D. Measurement without OBPF

The previous RF spectra are based on the specific longitudinal mode around 1555 nm via the optical bandpass filter. In this section, we investigate chaotic characteristics for the outputs of different longitudinal modes and all the modes. The full lasing spectra at the current of 35 mA are provided in Fig. 8(a). For longitudinal mode around 1557 nm, two main peaks can be identified at the wavelengths of 1556.700 and 1556.796 nm from the wide chaotic lasing spectrum. The mode interval is around 0.096 nm, corresponding to 12 GHz frequency. When this mode is filtered and detected by the high-speed PD, a peak at 12 GHz is observed in the RF spectrum, as shown in Fig. 8(b). For longitudinal mode around 1567 nm, three strongest peaks at 1566.880, 1566.980, and 1567.100 nm are distinguished in Fig. 8(a). After optical filtering, the corresponding RF spectrum is illustrated in Fig. 8(c). A sharp

peak at 27.5 GHz occurs, resulting from the beating between the mode of 1566.880 and 1567.100 nm. Meanwhile, a flat envelope ranging from 10 to 20 GHz is also found. When the output of all the modes is detected by the PD, a superposition power spectrum, including 12.5 and 27.5 GHz peaks, can be obtained, as shown in Fig. 8(d). In short, the nonlinear phenomena could be complex without optical filtering, because of the contribution of mode beating from all longitudinal and transverse modes, including near-degenerate modes.

4. CONCLUSION

In summary, we have proposed and systematically investigated irregular pulse packages and self-chaos route characteristics for a dual-mode circular-sided square microcavity laser, including the effect of near-degenerate modes. By designing the deformed square microcavity with suitable mode Q-factors and mode interval, we clearly verify the internal mode interactions for the generation of nonlinear dynamics through finely adjusting the mode interval with injection current. Irregular pulse packages caused by the mode beating of near-degenerate modes are observed, and successive route from periodic-one to periodic-three states to chaos is experimentally illustrated by increasing current. Chaos operation over a current range of 10 mA due to internal mode interaction is achieved, with the highest on-chip chaotic effective bandwidth of 22.4 GHz and the flatness of chaos power spectrum of ± 4 dB. In addition, chaotic output behaviors are studied for different longitudinal modes, which are expected as parallel chaos sources. The precise boundary control via mode engineering serves as an enriched control knob for exploring nonlinear dynamics of the deformed microcavity lasers. We envision that the solitary chaotic microlasers will greatly improve the resolution of chaos detection and the rate of a portable random bit generator and potentially open up the ability of optical reservoir computing and secure communication with a simplified system.
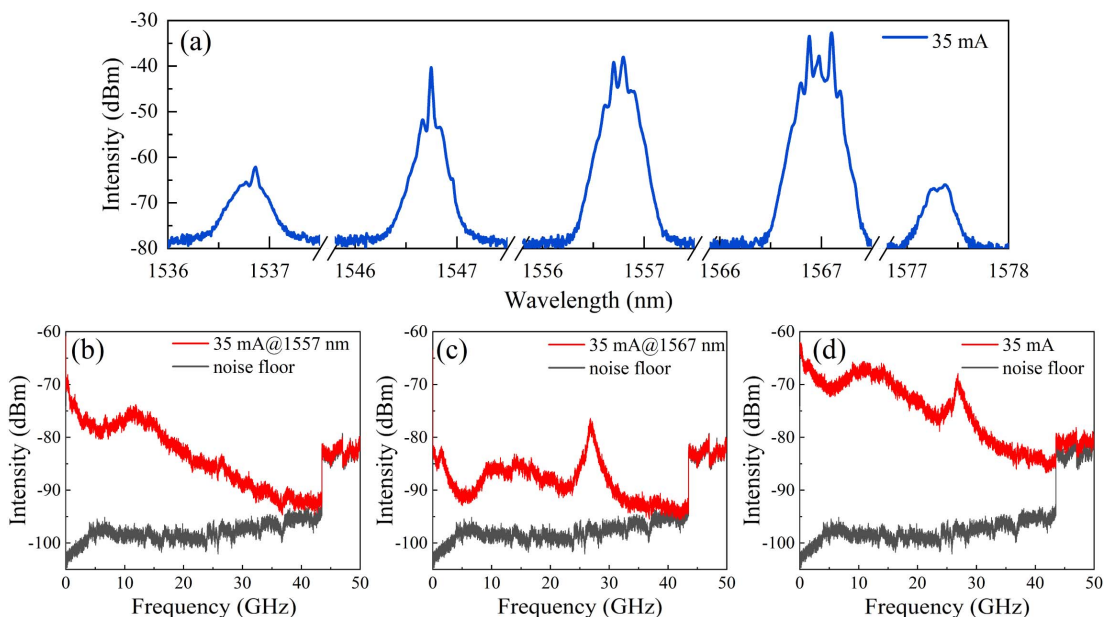

Fig. 8. (a) Full optical spectrum, and (b)–(d) RF spectrum at the current of 35 mA. RF spectra for (b) longitudinal mode around 1557 nm, (c) longitudinal mode around 1567 nm, and (d) all modes without optical filter.

Disclosures. The authors declare no conflicts of interest.

Data Availability. Data underlying the results presented in this paper are not publicly available at this time but may be obtained from the authors upon reasonable request.

REFERENCES

1. A. Uchida, K. Amano, M. Inoue, K. Hirano, S. Naito, H. Someya, I. Oowada, T. Kurashige, M. Shiki, S. Yoshimori, K. Yoshimura, and P. Davis, "Fast physical random bit generation with chaotic semiconductor lasers," Nat. Photonics **2**, 728–732 (2008).
2. Y. Guo, Q. Cai, P. Li, R. Zhang, B. Xu, K. A. Shore, and Y. Wang, "Ultrafast and real-time physical random bit extraction with all-optical quantization," Adv. Photon. **4**, 035001 (2022).
3. W. D. Shao, Y. D. Fu, M. F. Cheng, L. Deng, and D. M. Liu, "Chaos synchronization based on hybrid entropy sources and applications to secure communication," IEEE Photon. Technol. Lett. **33**, 1038–1041 (2021).
4. Y. H. Wang, M. J. Zhang, J. Z. Zhang, L. J. Qiao, T. Wang, Q. Zhang, L. Zhao, and Y. C. Wang, "Millimeter-level-spatial-resolution Brillouin optical correlation-domain analysis based on broadband chaotic laser," J. Lightwave Technol. **37**, 3706–3712 (2019).
5. C. H. Tseng and S. K. Hwang, "Broadband chaotic microwave generation through destabilization of period-one nonlinear dynamics in semiconductor lasers for radar applications," Opt. Lett. **45**, 3777–3780 (2020).
6. W. Z. Feng, N. Jiang, Y. Q. Zhang, J. Y. Jin, A. K. Zhao, S. Q. Liu, and K. Qiu, "Pulsed-chaos MIMO radar based on a single flat-spectrum and delta-like autocorrelation optical chaos source," Opt. Express **30**, 4782–4792 (2022).
7. Y. Kuriki, J. Nakayama, K. Takano, and A. Uchida, "Impact of input mask signals on delay-based photonic reservoir computing with semiconductor lasers," Opt. Express **26**, 5777–5788 (2018).
8. M. Sciamanna and K. A. Shore, "Physics and applications of laser diode chaos," Nat. Photonics **9**, 151–162 (2015).
9. J. Ohtsubo, *Semiconductor Lasers Stability, Instability and Chaos*, 4th ed. (Springer, 2017).
10. T. B. Simpson, J. M. Liu, A. Gavrielides, V. V. Kovanis, and P. M. Alsing, "Period-doubling route to chaos in a semiconductor laser subject to optical injection," Appl. Phys. Lett. **64**, 3539–3541 (1994).
11. T. B. Simpson, J. M. Liu, A. Gavrielides, V. V. Kovanis, and P. M. Alsing, "Period-doubling cascades and chaos in a semiconductor laser with optical injection," Phys. Rev. A **51**, 4181–4185 (1995).
12. Z. F. Jiang, Z. M. Wu, E. Jayaprasath, W. Y. Yang, C. X. Hu, and G. Q. Xia, "Nonlinear dynamics of exclusive excited-state emission quantum dot lasers under optical injection," Photonics **6**, 58 (2019).
13. L. Qiao, T. Lv, Y. Xu, M. Zhang, J. Zhang, T. Wang, R. Zhou, Q. Wang, and H. Xu, "Generation of flat wideband chaos based on mutual injection of semiconductor lasers," Opt. Lett. **44**, 5394–5397 (2019).
14. T. Mukai and K. Otsuka, "New route to optical chaos: successive-subharmonic-oscillation cascade in a semiconductor laser coupled to an external cavity," Phys. Rev. Lett. **55**, 1711–1714 (1985).
15. J. Mork, J. Mark, and B. Tromborg, "Route to chaos and competition between relaxation oscillations for a semiconductor laser with optical feedback," Phys. Rev. Lett. **65**, 1999–2002 (1990).
16. Y. Deng, Z. F. Fan, B. B. Zhao, X. G. Wang, S. Zhao, J. Wu, F. Grillot, and C. Wang, "Mid-infrared hyperchaos of interband cascade lasers," Light Sci. Appl. **11**, 7 (2022).
17. S. Tang and J. M. Liu, "Chaotic pulsing and quasi-periodic route to chaos in a semiconductor laser with delayed opto-electronic feedback," IEEE J. Quantum Electron. **37**, 329–336 (2001).
18. Y. H. Hong, P. S. Spencer, and K. A. Shore, "Wideband chaos with time-delay concealment in vertical-cavity surface-emitting lasers with optical feedback and injection," IEEE J. Quantum Electron. **50**, 236–242 (2014).
19. R. Zhang, P. Zhou, Y. Yang, Q. Fang, P. Mu, and N. Li, "Enhancing time-delay suppression in a semiconductor laser with chaotic optical injection via parameter mismatch," Opt. Express **28**, 7197–7206 (2020).
20. A. Argyris, M. Hamacher, K. E. Chlouverakis, A. Bogris, and D. Syvridis, "Photonic integrated device for chaos applications in communications," Phys. Rev. Lett. **100**, 194101 (2008).
21. V. Z. Tronciu, C. Mirasso, P. Colet, M. Hamacher, M. Benedetti, V. Vercesi, and V. Annovazzi-Lodi, "Chaos generation and synchronization using an integrated source with an air gap," IEEE J. Quantum Electron. **46**, 1840–1846 (2010).
22. T. Harayama, S. Sunada, K. Yoshimura, P. Davis, K. Tsuzuki, and A. Uchida, "Fast nondeterministic random-bit generation using on-chip chaos lasers," Phys. Rev. A **83**, 031803 (2011).
23. S. Sunada, T. Harayama, K. Arai, K. Yoshimura, P. Davis, K. Tsuzuki, and A. Uchida, "Chaos laser chips with delayed optical feedback using a passive ring waveguide," Opt. Express **19**, 5713–5724 (2011).
24. J. G. Wu, L. J. Zhao, Z. M. Wu, D. Lu, X. Tang, Z. Q. Zhong, and G. Q. Xia, "Direct generation of broadband chaos by a monolithic integrated semiconductor laser chip," Opt. Express **21**, 23358–23364 (2013).
25. M. J. Zhang, Y. H. Xu, T. Zhao, Y. N. Niu, T. Lv, Y. Liu, Z. K. Zhang, J. Z. Zhang, Y. Liu, Y. C. Wang, and A. B. Wang, "A hybrid integrated short-external-cavity chaotic semiconductor laser," IEEE Photon. Technol. Lett. **29**, 1911–1914 (2017).
26. M. Chai, L. Qiao, S. Li, X. Wei, H. Xu, J. Zhao, and M. Zhang, "Wavelength-tunable monolithically integrated chaotic semiconductor laser," J. Lightwave Technol. **40**, 5952–5957 (2022).
27. M. P. Vaughan, I. Henning, M. J. Adams, L. J. Rivers, P. Cannard, and I. F. Lealman, "Mutual optical injection in coupled DBR laser pairs," Opt. Express **17**, 2033–2041 (2009).
28. D. Liu, C. Sun, B. Xiong, and Y. Luo, "Nonlinear dynamics in integrated coupled DFB lasers with ultra-short delay," Opt. Express **22**, 5614–5622 (2014).
29. M. Tang, Y. D. Yang, J. L. Wu, Y. Z. Hao, H. Z. Weng, J. L. Xiao, and Y. Z. Huang, "Dynamical characteristics of twin-microring lasers with mutual optical injection," J. Lightwave Technol. **39**, 1444–1450 (2021).
30. M. Virte, K. Panajotov, H. Thienpont, and M. Sciamanna, "Deterministic polarization chaos from a laser diode," Nat. Photonics **7**, 60–65 (2012).
31. C. G. Ma, J. L. Xiao, Z. X. Xiao, Y. D. Yang, and Y. Z. Huang, "Chaotic microlasers caused by internal mode interaction for random number generation," Light Sci. Appl. **11**, 187 (2022).
32. J. C. Li, J. L. Xiao, Y. D. Yang, Y. L. Chen, and Y. Z. Huang, "Random bit generation based on self-chaotic microlasers with enhanced chaotic bandwidth," arXiv, arXiv:2301.00111v2 (2022).
33. J. C. Li, Y. L. Li, Y. X. Dong, Y. D. Yang, J. L. Xiao, and Y. Z. Huang, "400 Gb/s physical random number generation based on deformed square self-chaotic lasers," Chin. Opt. Lett. **21**, 061901 (2023).
34. Z. Z. Shen, M. Tang, Y. L. Chen, and Y. Z. Huang, "Unidirectional emission and nanoparticle detection in a deformed circular square resonator," Opt. Express **29**, 1666–1677 (2021).
35. H. E. Tureci, H. G. L. Schwefel, A. D. Stone, and E. E. Narimanov, "Gaussian-optical approach to stable periodic orbit resonances of partially chaotic dielectric micro-cavities," Opt. Express **10**, 752–776 (2002).
36. S. Wang, S. Liu, Y. Liu, S. Xiao, Z. Wang, Y. Fan, J. Han, L. Ge, and Q. Song, "Direct observation of chaotic resonances in optical microcavities," Light Sci. Appl. **10**, 135 (2021).
37. H. Long, Y. Z. Huang, X. W. Ma, Y. D. Yang, J. L. Xiao, L. X. Zou, and B. W. Liu, "Dual-transverse-mode microsquare lasers with tunable wavelength interval," Opt. Lett. **40**, 3548–3551 (2015).

38. L. A. Coldren, Scott W. Corzine, and M. L. Mashanovitch, *Diode Lasers and Photonic Integrated Circuits*, 2nd ed. (Wiley, 2012).
39. T. Heil, I. Fischer, W. Elsäßer, B. Krauskopf, K. Green, and A. Gavrielides, "Delay dynamics of semiconductor lasers with short external cavities: bifurcation scenarios and mechanisms," Phys. Rev. E **67**, 066214 (2003).
40. A. Tabaka, K. Panajotov, I. Veretennicoff, and M. Sciamanna, "Bifurcation study of regular pulse packages in laser diodes subject to optical feedback," Phys. Rev. E **70**, 036211 (2004).
41. F. Y. Lin, Y. K. Chao, and T. C. Wu, "Effective bandwidths of broadband chaotic signals," IEEE J. Quantum Electron. **48**, 1010–1014 (2012).
42. P. Li, Q. Cai, J. G. Zhang, B. J. Xu, Y. M. Liu, A. Bogris, K. A. Shore, and Y. C. Wang, "Observation of flat chaos generation using an optical feedback multi-mode laser with a band-pass filter," Opt. Express **27**, 17859–17867 (2019).
43. Y. Z. Hao, C. G. Ma, Z. Z. Shen, J. C. Li, J. L. Xiao, Y. D. Yang, and Y. Z. Huang, "Comparison of single- and dual-mode lasing states of a hybrid-cavity laser under optical feedback," Opt. Lett. **46**, 2115–2118 (2021).
44. C. G. Ma, J. L. Wu, J. L. Xiao, Y. T. Huang, Y. L. Li, Y. D. Yang, and Y. Z. Huang, "Wideband chaos generation based on a dual-mode microsquare laser with optical feedback," Chin. Opt. Lett. **19**, 111401 (2021).
45. Y. L. Li, C. G. Ma, J. L. Xiao, T. Wang, J. L. Wu, Y. D. Yang, and Y. Z. Huang, "Wideband chaotic tri-mode microlasers with optical feedback," Opt. Express **30**, 2122–2130 (2022).
46. B. Boashash, *Time-Frequency Signal Analysis and Processing*, 2nd ed. (Academic, 2016).
47. F. Tan, M. K. Wu, M. Liu, M. Feng, and N. Holonyak, "Relative intensity noise in high speed microcavity laser," Appl. Phys. Lett. **103**, 141116 (2013).